Physics of Plasmas

Effects of ion polarization and finite-β on heat transport in slab electron-temperature-gradient driven turbulence

Cite as: Phys. Plasmas **28**, 052512 (2021); https://doi.org/10.1063/5.0044435
Submitted: 18 January 2021 . Accepted: 03 May 2021 . Published Online: 25 May 2021

S. Maeyama, S. Kusaka, and T.-H. Watanabe

Physics of Plasmas ARTICLE scitation.org/journal/php

Effects of ion polarization and finite-β on heat transport in slab electron-temperature-gradient driven turbulence

Cite as: Phys. Plasmas **28**, 052512 (2021); doi: 10.1063/5.0044435
Submitted: 18 January 2021 · Accepted: 3 May 2021 ·
Published Online: 25 May 2021

View Online Export Citation CrossMark

S. Maeyama,[a] S. Kusaka, and T.-H. Watanabe

AFFILIATIONS

Department of Physics, Nagoya University, Nagoya 464-8602, Japan

[a]Author to whom correspondence should be addressed: smaeyama@p.phys.nagoya-u.ac.jp

ABSTRACT

Effects of kinetic ions and electromagnetic fluctuations on slab electron-temperature-gradient (ETG) driven turbulence are investigated by means of gyrokinetic simulations covering scales from electron gyroradius to ion gyroradius and electron skin depth. Linear growth rates of electrostatic ETG modes are enhanced by the ion polarization at ion gyroradius scale. Nonlinear simulations show that this low-poloidal-wavenumber instability induces ion-scale eddies which cause heat transport higher than that in the adiabatic ion model. In finite-β plasma, electromagnetic fluctuations stabilize the low-wavenumber modes, and suppress the turbulent heat transport. Additionally, electromagnetic effects also weaken zonal flow generation, which slightly enhances turbulent transport than that in the electrostatic adiabatic ion model.

I. INTRODUCTION

Suppression of turbulent heat transport in magnetically confined plasma is one of the key issues in fusion research. It is considered that one of the important instabilities to explain anomalous heat transport is ion temperature gradient (ITG) modes which drive turbulent eddies at the ion gyroradius scale. On the other hand, at the electron gyroradius scale, finer-scale instabilities like electron temperature gradient (ETG) modes should be taken into account.[1] Understanding of ETG turbulence and transport would also be important to burning plasma research, where collisions with fusion-born fast alpha particles mainly heat electrons.

ITG/ETG modes are classified into slab modes[2] and toroidal modes[3,4] depending on the destabilization mechanisms. Because of strong transport driven by the toroidal ETG turbulence, extensive simulation studies have been carried out based on gyrokinetics. In studies of the ETG turbulence, ion response was often assumed to be the Boltzmann response (i.e., ion density perturbations $\tilde{n}_\mathrm{i}$ proportional to perturbed electrostatic (ES) potential $\tilde{\phi}$), called the adiabatic ion model, because of the large difference between ion and electron gyroradii. Toroidal ETG turbulence with the adiabatic ion model often involves radially elongated structures, called streamers, and causes strong heat transport,[5,6] where zonal flows are considered to play a subsidiary role in contrast to the ITG turbulence. A recent study, however, pointed out the generation of zonal flows and a reduced level of transport in a long-time simulation of the toroidal ETG turbulence with the adiabatic ion response.[7] In addition, kinetic ion effects on the ETG turbulence have attracted the researcher's attention. Multi-scale simulations including both of ITG and ETG modes show that strong suppression of ETG turbulence due to shearing by ITG turbulent eddies.[8–12] Even without ITG mode fluctuations, the adiabatic and kinetic ion models have shown a discrepancy in the saturation levels of toroidal ETG turbulence,[8] which has not been entirely resolved yet.

Although the ETG modes at electron gyroradius scale are essentially electrostatic modes, there was an attempt to discuss the effects of the electromagnetic fluctuations,[13] where the appearance of large eddies of the order of electron skin depth was expected as a result of an inverse cascade of ETG turbulence. Similarly, electromagnetic fluctuations in ETG turbulence were also discussed in regard to the Ohkawa's electron heat transport scaling.[14,15] However, since the electron skin depth is much longer than the electron gyroradius in low-β plasma, many of the gyrokinetic simulation studies have focused on the ETG turbulence at electron gyroradius scale in electrostatic approximation.[7,8,16–18]

In this study, we investigate the effects of kinetic ions and electromagnetic fluctuations on shearless slab ETG driven turbulence. This model is associated with a local model in the vicinity of the minimum q surface in the reversed shear profile of tokamak discharges.[1,19] There is also increasing interest in the impact of ETG modes in the tokamak

H-mode pedestal, where the slab ETG modes are believed to play an important role.[20] It is known that the saturated state of slab ETG turbulence, e.g., quasi-steady zonal flows[19] or coherent vortex street structures,[21] is different from streamer-dominated toroidal ETG turbulence. The simple shearless slab model helps us to focus on the effect of nonadiabatic ions on ETG turbulence. We also exclude ITG mode fluctuations by setting a zero ion temperature gradient in the analysis. Since the nonadiabatic effect appears at ion gyroradius or electron skin depth scale, which is much larger than that of the most unstable ETG modes, we carry out nonlinear gyrokinetic simulations with enough large box size and fine resolutions.

The remainder of this paper is organized as follows. Section II explains governing equations of our model. Section III shows linear and nonlinear simulation results, where we compare four types of simulations: electrostatic/electromagnetic and adiabatic/kinetic ions. Finally, concluding remarks are given in Sec. IV.

II. MODEL EQUATIONS

A. Gyrokinetic electron/ion model

We consider nonlinear electromagnetic gyrokinetic equations[22,23] with equilibrium Maxwellian background F_{sM}. The perturbed distribution functions and electromagnetic potentials are written in terms of the Fourier expansions

$$\tilde{f}_{\mathrm{s}}(x,y,v_\parallel,\mu,t)=\sum_{k_x}\sum_{k_y}\tilde{f}_{\mathrm{s}\boldsymbol{k}}(v_\parallel,t)F_{\mathrm{sM}\perp}(\mu)e^{i(k_x x+k_y y)}, \tag{1}$$

$$\tilde{\phi}(x,y,t)=\sum_{k_x}\sum_{k_y}\tilde{\phi}_{\boldsymbol{k}}(t)e^{i(k_x x+k_y y)}, \tag{2}$$

$$\tilde{A}_\parallel(x,y,t)=\sum_{k_x}\sum_{k_y}\tilde{A}_{\parallel\boldsymbol{k}}(t)e^{i(k_x x+k_y y)}, \tag{3}$$

where we assume translational symmetry in the z-direction and Maxwell distribution of the perpendicular velocity dependence $F_{\mathrm{sM}\perp}=e^{-\mu B/T_{\mathrm{s}}}m_{\mathrm{s}}/(2\pi T_{\mathrm{s}})$ with mass m_{s}, equilibrium temperature T_{s}, and magnetic moment μ. The background magnetic field is uniform $\boldsymbol{B}=B(\hat{\boldsymbol{z}}+\theta\hat{\boldsymbol{y}})$ where $\theta\ll 1$ is a tilt angle of the field line,[24] so that there is neither mirror force nor magnetic drift. The scale lengths of density and temperature gradients in x-direction are $L_n=-(d\ln n/dx)^{-1}$ and $L_{T_{\mathrm{s}}}=-(d\ln T_{\mathrm{s}}/dx)^{-1}$, respectively. Integrating over the perpendicular velocity space, one obtains the gyrokinetic Vlasov equation in the perpendicular wavenumber space $\boldsymbol{k}_\perp=k_x\hat{\boldsymbol{x}}+k_y\hat{\boldsymbol{y}}$ and the parallel velocity space $v_\parallel$

$$\frac{\partial\tilde{f}_{\mathrm{s}\boldsymbol{k}}}{\partial t}+ik_\parallel v_\parallel\tilde{f}_{\mathrm{s}\boldsymbol{k}}+N_{\mathrm{s}\boldsymbol{k}}-C_{\mathrm{s}\boldsymbol{k}}=\frac{e_{\mathrm{s}}F_{\mathrm{sM}\parallel}}{T_{\mathrm{s}}}e^{-b_{\mathrm{s}\boldsymbol{k}}/2}\left[i\omega_{*T_{\mathrm{s}}}\left(\tilde{\phi}_{\boldsymbol{k}}-v_\parallel\tilde{A}_{\parallel\boldsymbol{k}}\right)-v_\parallel\left(ik_\parallel\tilde{\phi}_{\boldsymbol{k}}+\frac{\partial\tilde{A}_{\parallel\boldsymbol{k}}}{\partial t}\right)\right], \tag{4}$$

where the parallel wavenumber is given by $k_\parallel=\theta k_y$. The Maxwellian distribution in the parallel direction is denoted by $F_{\mathrm{sM}\parallel}=n\sqrt{m_{\mathrm{s}}/(2\pi T_{\mathrm{s}})}e^{-m_{\mathrm{s}}v_\parallel^2/(2T_{\mathrm{s}})}$ with equilibrium density $n_{\mathrm{e}}=n_{\mathrm{i}}=n$. The finite gyroradius effect after perpendicular velocity integration is denoted by $e^{-b_{\mathrm{s}\boldsymbol{k}}/2}$ with $b_{\mathrm{s}\boldsymbol{k}}=k_\perp^2\rho_{\mathrm{ts}}^2$, $\rho_{\mathrm{ts}}=v_{\mathrm{ts}}/\Omega_{\mathrm{s}}$, $v_{\mathrm{ts}}=\sqrt{T_{\mathrm{s}}/m_{\mathrm{s}}}$, $\Omega_{\mathrm{s}}=e_{\mathrm{s}}B/m_{\mathrm{s}}$ and electric charge $-e_{\mathrm{e}}=e_{\mathrm{i}}=e$. The diamagnetic drift frequency is $\omega_{*T_{\mathrm{s}}}=\omega_{*\mathrm{s}}[1+(\eta_{\mathrm{s}}/2)(m_{\mathrm{s}}v_\parallel^2/T_{\mathrm{s}}-1-b_{\mathrm{s}\boldsymbol{k}})]$ with $\omega_{*\mathrm{s}}=-T_{\mathrm{s}}k_y/(e_{\mathrm{s}}BL_n)$ and $\eta_{\mathrm{s}}=L_n/L_{T_{\mathrm{s}}}$. $N_{\mathrm{s}\boldsymbol{k}}$ and $C_{\mathrm{s}\boldsymbol{k}}$ represent the nonlinear advection and collision terms

$$N_{\mathrm{s}\boldsymbol{k}}=-\sum_{k_x'}\sum_{k_y'}\sum_{k_x''}\sum_{k_y''}\delta_{\boldsymbol{k}'+\boldsymbol{k}'',\boldsymbol{k}}\frac{k_x'k_y''-k_y'k_x''}{B}e^{-b_{\mathrm{s}\boldsymbol{k}'}/2}\times\left(\tilde{\phi}_{\boldsymbol{k}'}-v_\parallel\tilde{A}_{\parallel\boldsymbol{k}'}\right)\tilde{g}_{\mathrm{s}\boldsymbol{k}''}, \tag{5}$$

$$C_{\mathrm{s}\boldsymbol{k}}=\nu_{\mathrm{s}}\left[\frac{\partial}{\partial v_\parallel}\left(v_{\mathrm{ts}}^2\frac{\partial}{\partial v_\parallel}+v_\parallel\right)-k_\perp^2\rho_{\mathrm{ts}}^2\right]\tilde{g}_{\mathrm{s}\boldsymbol{k}}, \tag{6}$$

with $\tilde{g}_{\mathrm{s}\boldsymbol{k}}=\tilde{f}_{\mathrm{s}\boldsymbol{k}}+e_{\mathrm{s}}F_{\mathrm{sM}\parallel}e^{-b_{\mathrm{s}\boldsymbol{k}}/2}\tilde{\phi}_{\boldsymbol{k}}/T_{\mathrm{s}}$ and the Kronecker's delta $\delta_{i,j}$. Small but finite collision frequency is modeled by a constant ν_{s}. Perturbed electromagnetic potentials are determined by the quasi-neutrality

$$\tilde{n}_{\mathrm{e}\boldsymbol{k}}=\tilde{n}_{\mathrm{i}\boldsymbol{k}}, \tag{7}$$

$$\tilde{n}_{\mathrm{s}\boldsymbol{k}}=e^{-b_{\mathrm{s}\boldsymbol{k}}/2}\int\tilde{f}_{\mathrm{s}\boldsymbol{k}}dv_\parallel-\frac{e_{\mathrm{s}}n}{T_{\mathrm{s}}}(1-\Gamma_{0\mathrm{s}\boldsymbol{k}})\tilde{\phi}_{\boldsymbol{k}}, \tag{8}$$

and the Ampère equation

$$k_\perp^2\tilde{A}_{\parallel\boldsymbol{k}}=\mu_0\sum_{\mathrm{s=e,i}}\tilde{j}_{\parallel\mathrm{s}\boldsymbol{k}}, \tag{9}$$

$$\tilde{j}_{\parallel\mathrm{s}\boldsymbol{k}}=e_{\mathrm{s}}e^{-b_{\mathrm{s}\boldsymbol{k}}/2}\int v_\parallel\tilde{f}_{\mathrm{s}\boldsymbol{k}}dv_\parallel, \tag{10}$$

where $\Gamma_{0\mathrm{s}\boldsymbol{k}}=I_0(b_{\mathrm{s}\boldsymbol{k}})e^{-b_{\mathrm{s}\boldsymbol{k}}}$ with the zeroth-order modified Bessel function I_0. The present model of shearless slab ETG with kinetic ion model is an electromagnetic extension of Ref. 25.

B. Gyrokinetic electron and adiabatic ion model

Since typical scale of ETG is at electron gyroradius $k_\perp\sim\rho_{\mathrm{te}}^{-1}$, one takes a limit of $k_\perp\rho_{\mathrm{ti}}\gg 1$ which simplifies the ion response to ETG fluctuations, called the adiabatic ion model. Ion parallel current at ETG scale perturbations are negligible due to ion gyroaveraging $\tilde{j}_{\parallel\mathrm{i}\boldsymbol{k}}\propto e^{-b_{\mathrm{i}\boldsymbol{k}}}\to 0$, and ion density becomes the Boltzmann response under $\Gamma_{0\mathrm{i}\boldsymbol{k}}\to 0$

$$\tilde{n}_{\mathrm{i}\boldsymbol{k}}=-\frac{en}{T_{\mathrm{i}}}\tilde{\phi}_{\boldsymbol{k}}. \tag{11}$$

Hence, kinetic ion response is decoupled from electron-scale equations. Electron gyrokinetic Eqs. (4)–(10) with $\tilde{j}_{\parallel\mathrm{i}\boldsymbol{k}}=0$ and Eq. (11) close the set of equations. The shearless slab ETG model with the adiabatic ion response is an electromagnetic extension of Ref. 21.

III. EFFECTS OF KINETIC IONS AND ELECTROMAGNETIC PERTURBATIONS ON ETG

Since linear ETG instability is essentially electrostatic, simple analyses of ETG turbulence have been done under the adiabatic ion model and electrostatic approximation. To investigate the effects of kinetic ions and electromagnetic fluctuations, we compare simulation results of four different models, namely, combinations of adiabatic/kinetic ions and electrostatic/electromagnetic models (EM). The nonadiabatic ion response is expected to be important at scales similar to or larger than the ion gyroradius ρ_{ti}. Similarly, the electromagnetic fluctuations are important at scales larger than electron skin depth $d_{\mathrm{e}}=c/\omega_{\mathrm{pe}}=\rho_{\mathrm{te}}/\sqrt{\beta}$ with the electron $\beta=\mu_0 nT_{\mathrm{e}}/B^2$.

In the following, the plasma parameters are set to be $T_i/T_e = 1$, $\eta_e = 10$, $\eta_i = 0$, $\Theta = \theta L_n/\rho_{te} = 0.5$, $\nu_s = 0.01$, $m_i/m_e = 750$, and $\beta = 0.002$. For these parameters, the ratio of ion and electron gyroradii is $\rho_{ti}/\rho_{te} = \sqrt{m_i T_i/(m_e T_e)} \sim 27.4$, and the ratio of electron skin depth and electron gyroradius is $d_e/\rho_{te} = \beta^{-1/2} = 22.4$.

A. Dispersion relation of linear ETG modes

Neglecting N_{sk} and C_{sk} from Eqs. (4)–(10), one derives the linear dispersion relation of the collisionless ETG modes for kinetic ion model with electromagnetic fluctuations. Figure 1 plots the linear growth rate of ETG modes obtained from the models in Sec. II. The maximum growth rate of ETG is $\gamma_{l,\max} = 0.38 v_{te}/L_n$ at $k_\perp = 0.73\rho_{te}^{-1} = 20\rho_{ti}^{-1} = 16 d_e^{-1}$, which is not affected by the choice of the models, since $k_\perp \gg \rho_{ti}^{-1}, d_e^{-1}$ is well satisfied. From the comparison with adiabatic/kinetic ion models in electrostatic approximation, the growth rate at lower wavenumber $k_\perp < 0.05\rho_{te}^{-1} = 1.37\rho_{ti}^{-1}$ is enhanced due to the nonadiabatic ion response. However, these are suppressed when electromagnetic fluctuations are taken into account. The electromagnetic stabilization occurs around $k_\perp \sim 0.1\rho_{te}^{-1} = 2.7\rho_{ti}^{-1} = 2.2 d_e^{-1}$.

Because of reduction of μ dependence in Sec. II, the dispersion relation is slightly different from that given by the gyrokinetic equations with full μ dependence. Although the details are discussed in Appendixes A and B, the results of this section are unchanged. For the sake of generality, we explain the stability properties found in Fig. 1 by means of the linear dispersion relation of the gyrokinetic equations with full μ dependence (see the Appendix A)

$$\left[\sum_{s=e,i}\frac{2\alpha_s^2}{k_\perp^2 d_s^2}\left(1-\breve{G}_{0s}\right)\right]\left[1+\sum_{s=e,i}\frac{2\alpha_s^2}{k_\perp^2 d_s^2}\breve{G}_{2s}\right] + \left[\sum_{s=e,i}\frac{2\alpha_s^2}{k_\perp^2 d_s^2}\breve{G}_{1s}\right]^2 = 0, \tag{12}$$

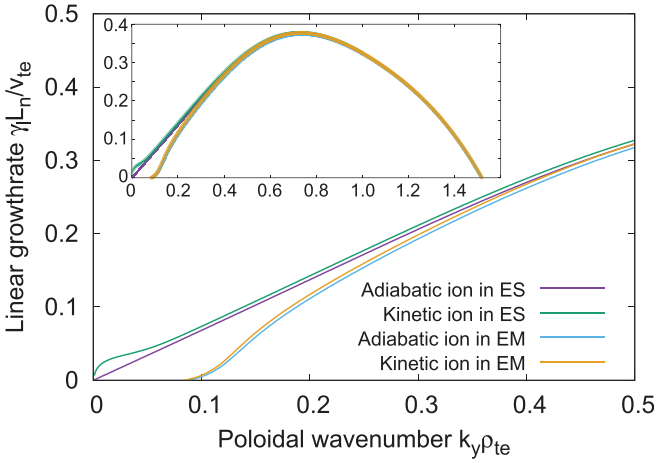

FIG. 1. Linear growth rate γ_l as functions of the poloidal wavenumber k_y obtained from the models in Sec. II. Violet, green cyan, and orange lines correspond to the results given by electrostatic adiabatic ion model [Eq. (11) and $\tilde{A}_{\parallel k} = 0$], electrostatic kinetic ion model ($\tilde{A}_{\parallel k} = 0$), electromagnetic adiabatic ion model [Eq. (11)], electromagnetic kinetic ion model, respectively.

$$\breve{G}_{1s} = \breve{G}_{2s} = \breve{G}_{0s} - \Gamma_{0sk}\left[1-\frac{\omega_{*s}}{\omega}\left(1-\frac{\eta_s \breve{b}_{sk}}{2}\right)\right], \tag{13}$$

$$\breve{G}_{0s} = \Gamma_{0sk}\Big\{-\alpha_s Z(\alpha_s) + \alpha_{*s} Z(\alpha_s) + \alpha_{*T_s}\left[\alpha_s(1+\alpha_s Z(\alpha_s)) - \frac{1}{2}\left(1+\breve{b}_{sk}\right)Z(\alpha_s)\right]\Big\}, \tag{14}$$

where $\breve{b}_{sk} = 2b_{sk}(1 - I_{1sk}/I_{0sk})$ with $I_{jsk} = I_j(b_{sk})$ and the jth-order modified Bessel function I_j. The normalized frequencies are given by $\alpha_s = \omega/(\sqrt{2}k_\parallel v_{ts})$, $\alpha_{*s} = \omega_{*s}/(\sqrt{2}k_\parallel v_{ts})$ and $\alpha_{*T_s} = \eta_s \alpha_{*s}$ for each particle species s, and the plasma dispersion function is denoted by Z.

For electrostatic approximation, one takes $\beta \to 0$ (equivalently $d_s^{-1} \to 0$) limit of Eq. (12) and obtains the dispersion relation for electrostatic kinetic ion model

$$1 - \breve{G}_{0e} = -\frac{T_e}{T_i}\left(1-\breve{G}_{0i}\right), \tag{15}$$

preserving the form of the quasi-neutrality condition in Eq. (7). The nonadiabatic response appears from the term of $\breve{G}_{ji}$. In the adiabatic ion model for $k_\perp \rho_{ti} \gg 1$, ion finite gyroradius terms are neglected $\Gamma_{0ik} = \breve{G}_{ji} = 0$, and the ion term is given only by the Boltzmann response $-T_e/T_i$.

The effects of kinetic ions and electromagnetic fluctuations on linear ETG modes are understood by a reduced dispersion relation in the following discussion. First, since the perpendicular wavenumber is in the range $\rho_{ti}^{-1} \lesssim k_\perp \ll \rho_{te}^{-1}$, one considers the drift kinetic limit for electrons $\Gamma_{0ek} = e^{-b_{ek}} = 1$ and $k_\perp^2 \rho_{te}^2 = 0$. However, we retain ion finite Larmor radius (FLR) effect Γ_{0sk} at full order of $k_\perp \rho_{ti}$. Second, taking a fluid limit of electrons $v_{te} \ll \omega/k_\parallel$, expand the electron plasma dispersion function as

$$Z(\alpha_e) = -\frac{1}{\alpha_e} - \frac{1}{2\alpha_e^3} - \frac{3}{4\alpha_e^5} + \mathcal{O}(\alpha_e^{-7}). \tag{16}$$

We note that this nonresonant limit is not applicable to the case when ETG mode is stabilized $v_{te} \sim \omega/k_\parallel$. The same expansion is applied to the ion plasma dispersion function, keeping only the lowest order term because of $\alpha_i^{-1} \ll \alpha_e^{-1}$. Then, one finds

$$\breve{G}_{0i} = \Gamma_{0ik}\left[1-\frac{\omega_{*i}}{\omega}\left(1-\frac{\eta_i \breve{b}_{ik}}{2}\right)\right] + \mathcal{O}(\alpha_i^{-2}), \tag{17}$$

$$\breve{G}_{1i} = \breve{G}_{2i} = \mathcal{O}(\alpha_i^{-2}), \tag{18}$$

which means that ion parallel motion is negligible in the electron gyroradius scale. In other words, the ion contribution is given by the polarization $1 - \Gamma_{0ik}$ with modification by the diamagnetic drift term of gyrocenter density

$$\tilde{n}_{ik} = -\frac{en}{T_i}\tilde{\phi}_k\left\{1-\Gamma_{0ik}\left[1-\frac{\omega_{*i}}{\omega}\left(1-\frac{\eta_i \breve{b}_{ik}}{2}\right)\right]\right\}, \tag{19}$$

$$\tilde{j}_{\parallel ik} = 0. \tag{20}$$

We here refer to the above as the FLR ion model. Third, for simplicity, we assume a flat density profile $1/L_n \sim 0$ and $T_i = T_e$. As a result, the

dispersion relation is reduced to that given by the fluid electrons and the ion polarization

$$\left[1+\frac{1}{k_\perp^2 d_e^2}\left(1-\frac{\alpha_{*T_e}}{\alpha_e}\right)\right]\left(1-\breve{G}_{0i}\right)-\frac{1}{2\alpha_e^2}\left(1-\frac{\alpha_{*T_e}}{\alpha_e}\right)=0, \quad (21)$$

which is consistent with Eq. (7) in Ref. 26 with $1/L_n \sim 0$, $T_i = T_e$, and neglecting grad-B and magnetic curvature. In contrast to Ref. 26, where ion was adiabatic $\breve{G}_{0i} \to 0$ and electron polarization $1-\Gamma_{0e\boldsymbol{k}} \to k_\perp^2\rho_{te}^2$ was retained for $k_\perp \lesssim \rho_{te}^{-1}$, we here consider $\rho_{ti}^{-1} \lesssim k_\perp \ll \rho_{te}^{-1}$ with the ion FLR terms but not for electrons. Each term in Eq. (21) can be related to that in the equation of electron fluid motion: the first term in the square brackets is the electron inertia, the second term is the induced electric field, and the third term proportional to $\alpha_{*T_e}/(k_\perp^2 d_e^2\alpha_e)$ is the electromagnetic diamagnetic effect. The factor of $1-\breve{G}_{0i}$ means the ion FLR correction by the polarization and diamagnetic drift. The second term from the last stems from the parallel electrostatic field, and the last term is the parallel gradient of electron pressure. Details on the relation to fluid equation are discussed in Appendix C.

The validity of the FLR ion model and the fluid electron approximation is examined in Fig. 2. The FLR ion model shows almost exact agreement with the full gyrokinetic result. The fluid electron model also captures the essential features, that is, destabilization by the ion FLR effect at low k_y and stabilization by the electromagnetic effect. It is noted that in the fluid model of Eq. (21), the diamagnetic drift terms are neglected so that the ion FLR effect is merely given by the ion polarization $\breve{G}_{0i} = \Gamma_{0s\boldsymbol{k}}$. Results shown in Fig. 2 are consistent with those in Fig. 1 with the reduced model equation for the μ dependence, where the ion polarization leads to enhancement of the ETG growth.

If we also apply a steep electron temperature gradient approximation $1 \ll \alpha_{*T_e}/\alpha_e$, Eq. (21) results in

$$\alpha_e^3-\frac{\alpha_{*T_e}}{k_\perp^2 d_e^2}\alpha_e^2+\frac{\alpha_{*T_e}}{2(1-\breve{G}_{0i})}=0, \quad (22)$$

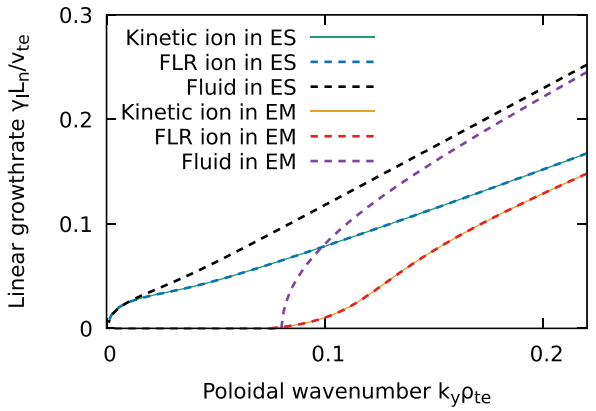

FIG. 2. Linear growth rate γ_l as functions of the poloidal wavenumber k_y. Solid orange, red dashed, and violet dashed lines correspond to the results given by electromagnetic gyrokinetic electron/ion model [Eq. (12)], gyrokinetic electron and FLR ion model [Eq. (12) with Eqs. (17) and (18)], fluid electron and FLR ion model [Eqs. (21) and (17)], respectively. Solid green, cyan dashed, and black dashed lines are the models same above, but in the electrostatic approximation $\beta = 0$.

which consists of the electron inertia, the electromagnetic diamagnetic term (steming from $\tilde{\boldsymbol{B}}\cdot\nabla P/B$), and the parallel gradient of perturbed electron pressure (i.e., $\nabla_\parallel\tilde{p}_e$) divided by the ion FLR factor $(1-\breve{G}_{0i})$. In the case that $\breve{G}_{0i}$ is approximated by $\Gamma_{0i\boldsymbol{k}}$, Eq. (22) is written as a cubic equation for $\omega = \alpha_e\sqrt{2}k_\parallel v_{te}$. In the electrostatic limit ($\beta = 0$ or $d_e^{-1} \to 0$), an instability is driven by the electron temperature gradient through the electron inertia and the parallel compression $\alpha_e^3 = -\alpha_{*T_e}/[2(1-\breve{G}_{0i})]$ for the wave propagating with $\alpha_{*T_e} > 0$, which is a well-known mechanism of destabilization of the electrostatic slab ETG mode [e.g., Eq. (5) in Ref. 27 for slab ETG, which is isomorphic to Eq. (3.91) of slab ITG in Ref. 28]. Considering ETG modes ($\omega_{*i}/\omega < 0$) at low $k_\perp$ ($1-\eta_i\breve{b}_{i\boldsymbol{k}}/2 > 0$), the ion FLR factor $1-\breve{G}_{0i} < 1$ modifies the electric field, which increases the magnitude of complex frequency, namely, enhances both of linear growth rate and real frequency. In the electromagnetic case, the diamagnetic term can stabilize the slab ETG modes.[26–28] A condition providing three stable real roots of ω in Eq. (22) determines the criteria for electromagnetic stabilization of ETG, that is,

$$\beta > \frac{3k_\perp^2\rho_{te}^2}{2\alpha_{*T_e}^{2/3}(1-\breve{G}_{0i})^{1/3}}. \quad (23)$$

The electromagnetic stabilization of ETG is found even in the adiabatic ion case ($\breve{G}_{0i} = 0$). The critical wavenumber of stabilization is given by $k_\perp^2 < k_{\perp,c}^2 = 2\alpha_{*Te}^{2/3}/(3d_e^2)$. Substituting the present parameters, $\alpha_{*T_e} = \eta_e/(\sqrt{2}\Theta) = 10\sqrt{2}$ and $d_e = 22.4\rho_{te}$, one estimates $k_{\perp,c} = 1.97d_e^{-1} = 0.088\rho_{te}^{-1}$, which shows a good agreement with the critical wavenumber of the slab ETG instability with electromagnetic fluctuations in Fig. 1.

Through the present linear analysis, we have found that one of the important nonadiabatic ion effects is the ion FLR polarization (with modification by diamagnetic drift of gyrocenter density), which reduces the effective dielectricity than that in the adiabatic ion model. As a result, both of linear growth rate and real frequency of ETG modes at $k_\perp \sim \rho_{ti}^{-1}$ increase. On the other hand, the electromagnetic effect stabilizes the ETG modes mainly through the diamagnetic term ($\tilde{\boldsymbol{B}}\cdot\nabla P/B$), which partially cancels parallel gradient of perturbed electron pressure ($\nabla_\parallel\tilde{p}_e$). Since the critical wavenumber of stabilization is proportional to the inverse of electron skin depth $k_{\perp,c} \sim d_e^{-1}$, low-$k_\perp$ ETG modes are stabilized as the plasma β increases.

B. Nonlinear simulations of ETG turbulence

In numerical simulations of ETG turbulence, time integration is carried out by means of the fourth-order Runge–Kutta–Gill method and the fourth-order central finite difference methods are used for evaluating the velocity-space derivatives in the collision operator. The nonlinear advection term is calculated by means of the spectral method with the 3/2-rule for de-aliasing in the wavenumber space. The simulation domain is set to be square with $L_x = L_y = 160\pi\rho_{te} (= 18.3\rho_{ti} = 22.4d_e)$, and $-5v_{te} \le v_\parallel \le 5v_{te}$. The phase-space resolution is set to be $(N_x, N_y, N_{v_\parallel}) = (1024, 1024, 512)$. Hereafter, physical quantities are normalized as $x = x'/\rho_{te}, y = y'/\rho_{te}, v_\parallel = v_\parallel'/v_{te}, t = t'v_{te}/L_n, \nu_s = \nu_s'L_n/v_{te}, F_{sM\parallel} = F_{sM\parallel}'v_{ts}/n, f_{s\boldsymbol{k}} = f_{s\boldsymbol{k}}'v_{ts}L_n/(n\rho_{te})$, $\tilde{\phi}_{\boldsymbol{k}} = \tilde{\phi}_{\boldsymbol{k}}eL_n/(T_e\rho_{te})$, and $\tilde{A}_{\parallel\boldsymbol{k}} = \tilde{A}_{\parallel\boldsymbol{k}}'ev_{te}L_n/(T_e\rho_{te})$, where the prime means dimensional quantities. The plasma parameters are the same as those used for the linear analysis.

Figure 3 plots the electron heat diffusivity

$$\chi_e = \frac{L_{T_e}}{nT_e}\sum_{k_x}\sum_{k_y}\mathrm{Re}\left[-\frac{ik_y e^{-b_{sk}/2}\tilde{\phi}_{\boldsymbol{k}}}{2B}\int\left(\frac{v_\parallel^2}{v_{te}^2}-1-b_{ek}\right)\tilde{f}_{ek}^* dv_\parallel\right], \tag{24}$$

for the adiabatic/kinetic ion and electrostatic/electromagnetic models. Initial growths found in all models are similar for $t < 50L_n/v_{te}$, since the most unstable mode at $k_\perp \sim 0.73\rho_{te}^{-1}$ is not influenced by the ion or electromagnetic responses. After the initial saturation of $50 < tv_{te}/L_n < 150$, χ_{te} in the electrostatic adiabatic ion model slowly decreases till $t \sim 800L_n/v_{te}$, which is associated with slow development of zonal flows as discussed in Refs. 7 and 21. Although the initial saturation level for the kinetic ion case is similar to that of the adiabatic ion one, the secondary growth of χ_{te} is observed after $t \sim 200L_n/v_{te}$, where the linear growth rates of low-k_y modes are enhanced by the ion polarization. Finally, the heat flux in electrostatic kinetic ion model exceeds $\chi_e \sim 100v_{te}\rho_{te}^2/L_n$ in the electron gyro-Bohm unit. Moderate levels of heat flux are observed in the cases with the adiabatic/kinetic ion response and electromagnetic fluctuations, but no secondary growth of low-k_y modes due to electromagnetic stabilization. In addition, no slow decrease in the heat flux is observed in contrast to the electrostatic adiabatic ion model, which suggests a difference in the zonal flow generation between the electrostatic and electromagnetic models. In the electromagnetic cases, the kinetic ion model gives slightly higher heat flux (about 15%) than that of the adiabatic ion one.

Snapshots of the electrostatic potential at $t = 800L_n/v_{te}$ in each model are shown in Fig. 4. Small isotropic vortices and zonal flow structures of wavelength $\sim 30\rho_{te}$ dominate in the electrostatic adiabatic ion model [Fig. 4(a)]. Since the adiabatic ion model does not contain the ion gyroradius scale ρ_{ti} and the electrostatic approximation excludes the electron skin depth scale d_e, the characteristic scales of vortices and zonal flows are governed only by electron dynamics, such as the Rhines scale of ETG turbulence.[29,30] On the other hand, large scale fluctuations of the order of the simulation box size, $k_\perp = 0.0125\rho_{te}^{-1} = 0.34\rho_{ti}^{-1}$, appear in case with kinetic ions [Fig. 4(b)]. The long wavelength modes are destabilized by the ion polarization and drive the extremely strong heat transport. These low-k_y modes are stabilized in the electromagnetic case [Fig. 4(d)]. As a results, typical scales of adiabatic/kinetic ion and electromagnetic models (c) and (d) are similar to (a), $\sim 30\rho_{te} \sim \rho_{ti} \sim d_e$.

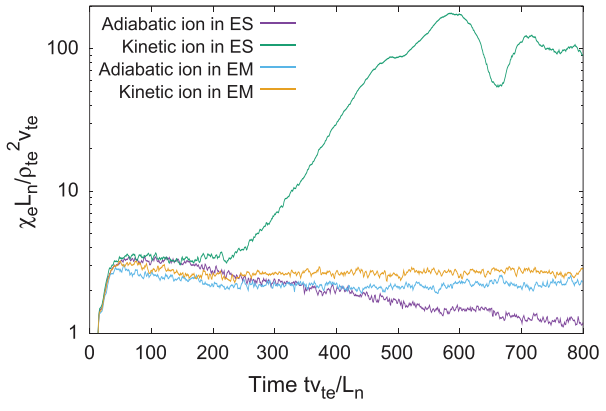

FIG. 3. Time evolution of electron heat diffusivity χ_e. Violet, green, cyan, and orange lines correspond to the results from electrostatic adiabatic ion, electrostatic kinetic ion, electromagnetic adiabatic ion, and electromagnetic kinetic ion models, respectively.

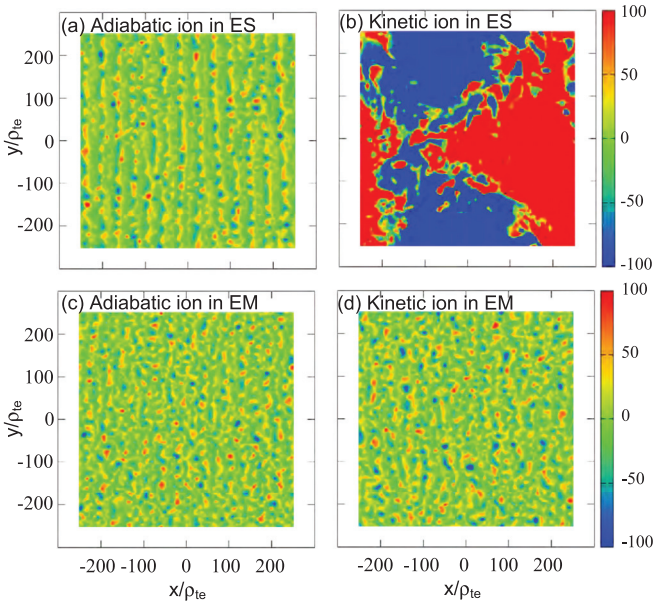

FIG. 4. Color contours of electrostatic potential $\tilde{\phi}(x, y)$ (normalized by $(\rho_{te}/L_n)T_e/e$) at $t = 800L_n/v_{te}$ are plotted for (a) electrostatic adiabatic ion, (b) electrostatic kinetic ion, (c) electromagnetic adiabatic ion, and (d) electromagnetic kinetic ion models, respectively.

More detailed differences are found in spectra of electrostatic field energy

$$W_{\boldsymbol{k}} = \sum_{s=e,i}\frac{e_s^2 n}{T_s}(1-\Gamma_{0s\boldsymbol{k}})\frac{|\tilde{\phi}_{\boldsymbol{k}}|^2}{2}, \tag{25}$$

in wavenumber space. In Fig. 5(a), one clearly see distinct peaks of $k_y = 0$ zonal flows in the electrostatic adiabatic ion model. From conventional understandings,[31] shearing by zonal flows stabilizes turbulent fluctuations. As zonal flows slowly develop, we have observed a continuous decrease in turbulent transport in Fig. 3. On the other hand, zonal flows are weakened in the electromagnetic cases [see Figs. 5(c) and 5(d)], where the energy spectra are more isotropic with faint peaks of zonal flows. It suggests that a finite-β effect weakens the zonal flow generation, probably, due to partial cancelation of the Reynolds stress drive by the Maxwell stress.[32] Poloidal wavenumbr (k_y) spectra of the field energy in Fig. 6 show the difference more clearly. There is a significant peak of $k_y = 0$ zonal flows in the electrostatic adiabatic ion model. On the other hand, in the electromagnetic case, zonal flow component is reduced, and $k_y \neq 0$ turbulent components are enhanced from those in the electrostatic case.

Poloidal wavenumber spectra of the electron heat flux are shown in Fig. 7 for the adiabatic/kinetic ion and electromagnetic models. Although the linear growth rates are almost identical (see Fig. 1), low-k_y ($k_y \sim 0.1\rho_{te}^{-1} \sim 2.7\rho_{ti}^{-1}$) components of the heat flux in the

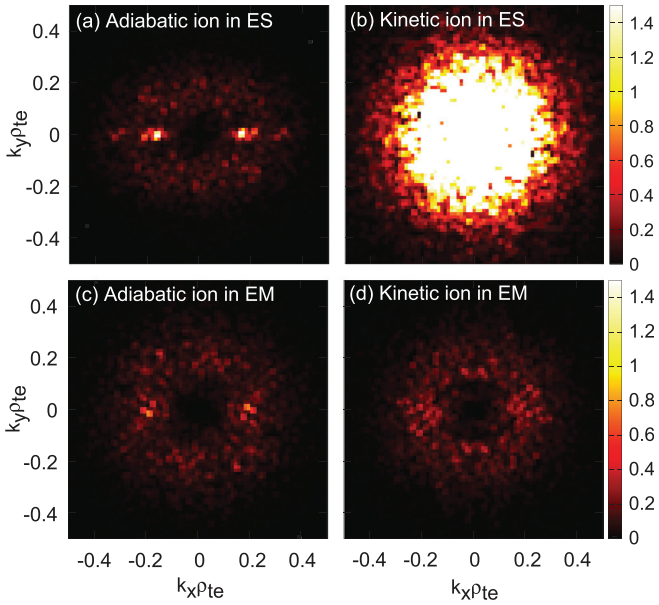

FIG. 5. Color contours of electrostatic field energy spectra $W_{\boldsymbol{k}}$ (normalized by $(\rho_{te}/L_n)^2 nT_e$) in wavenumber space at $t = 800L_n/v_{te}$ for (a) electrostatic adiabatic ion, (b) electrostatic kinetic ion, (c) electromagnetic adiabatic ion, and (d) electromagnetic kinetic ion models, respectively.

turbulent state of the kinetic ion model are higher than those of the adiabatic ion model. As discussed in the linear theory, Sec. III A, an important nonadiabatic ion effect is the ion polarization which enhances the electrostatic potential fluctuation such that $\tilde{\phi}_{\boldsymbol{k}} \sim -\tilde{n}_e T_i/(en)$ to $\tilde{\phi}_{\boldsymbol{k}} \sim -\tilde{n}_e T_i/[en(1-\bar{G}_{0i})]$. Since the effect is valid even in the nonlinear turbulence, we conclude that the ion polarization enhances low-k_y components of ETG turbulence.

It is noteworthy that the linear growth rates in Fig. 1 are on the order of (AiEM) $\lesssim$ (KiEM) $<$ (AiES) $<$ (KiES), where Ai, Ki, ES, and

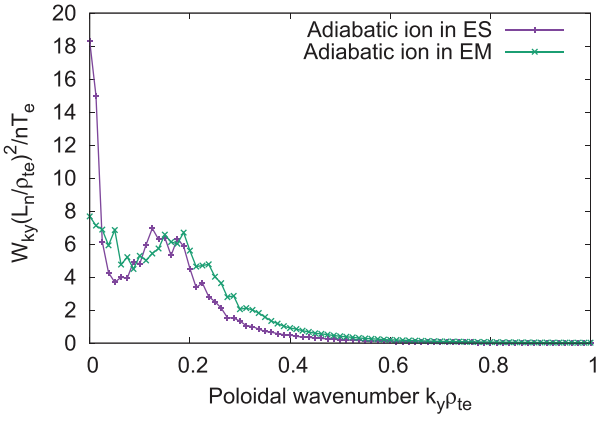

FIG. 6. Electrostatic field energy as functions of poloidal wavenumber k_y, summed over radial wavenumbers $W_{k_y} = \sum_{k_x} W_{\boldsymbol{k}}$ at $t = 800L_n/v_{te}$. Results of adiabatic ion and electrostatic/electromagnetic models are plotted in violet and green lines, respectively.

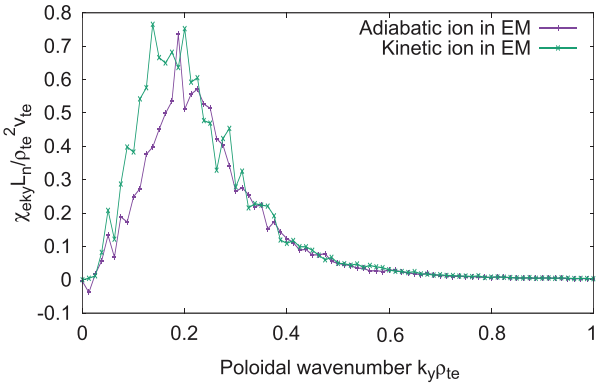

FIG. 7. Electron heat diffusivity as functions of poloidal wavenumber k_y at $t = 800L_n/v_{te}$. Results of adiabatic/kinetic ion and electromagnetic models are plotted in violet and green lines, respectively.

EM are the abbreviations of adiabatic ion, kinetic ion, electrostatic, and electromagnetic models, respectively. Nevertheless, magnitudes of the turbulent transport in Fig. 3 are on the order of (AiES) $\ll$ (AiEM) $\lesssim$ (KiEM) $\ll$ (KiES). Generation of the zonal flows is responsible for the reduced transport in AiES model, while it is weakened in EM cases. It is also confirmed that the low-$k_\perp$ ETG modes destabilized in KiES model have the significant impact on the heat flux.

C. Discussions on turbulent spectra

Let us try to understand the formation of turbulent energy spectra as a competition among five inherent scale lengths k_l^{-1}, k_R^{-1}, k_q^{-1}, k_d^{-1}, and k_i^{-1}, defined below. The first scale $k_l^{-1} \sim \rho_{te}$ is the electron gyroradius, which characterizes the scale of linear ETG instability. The subsequent two scales are derived in analogy with the Hasegawa–Mima equation.[33] Considering finite amplitude of turbulent fluctuations $U \sim |\nabla\tilde{\phi}/B|$, one finds the second scale k_R^{-1} that the nonlinear turbulent mixing rate balances with the linear wave dispersion, which is called the Rhines scale[34] $k_R\rho_{te} \sim \sqrt{\rho_{te}v_{te}/(L_nU)}$. The third scale k_q^{-1} is related to the adiabatic ion response in Poisson equation $(T_e/T_i + k_\perp^2\rho_{te}^2)\tilde{\phi} = \int \tilde{f}_{e\boldsymbol{k}} dv_\parallel$, where the long-wavelength approximation $k_\perp\rho_{te} \ll 1$ is employed. Although it resembles the relation between potential and vorticity in the 2D Navier–Stokes equation $k_\perp^2\tilde{\phi} = \omega$, the adiabatic ion response makes a difference in the long-wavelength behavior of the Hasegawa–Mima equation. At the long-wavelength scale of $k_\perp^2\rho_{te}^2 \ll T_e/T_i$, the potential in Hasegawa–Mima equation ($\tilde{\phi} \propto T_i/T_e$) becomes much smaller than that in 2D Navier–Stokes equation [$\tilde{\phi} \propto 1/(k_\perp^2\rho_{te}^2)$]. As a result, in the Hasegawa–Mima system inverse cascade slows down at $k_\perp^2\rho_{te}^2 \ll T_e/T_i$, where the characteristic scale is called the scale of quasi-crystallization,[35] $k_q\rho_{te} \ll \sqrt{T_e/T_i}$. (When one considers the nonadiabatic ion polarization, it is modified to $k_q\rho_{te} \ll \sqrt{(1-\Gamma_{0i\boldsymbol{k}})T_e/T_i}$.) Though the above three scales appear even in the electrostatic adiabatic ion model, the fourth scale of the electron skin depth $k_d^{-1} \sim d_e$ and the fifth scale of ion gyroradius $k_i^{-1} \sim \rho_{ti}$ provide typical scales of electromagnetic and kinetic ion effects, respectively.

Correspondence of the Rhines and quasi-crystallization scales k_R^{-1} and k_q^{-1} to the formation of turbulent energy spectra in slab ETG turbulence was investigated in Ref. 30, where the inverse energy

cascade is prevented around either k_R or k_q, determined by the competition of k_R/k_q. Because of the anisotropic dispersion of the drift waves, the dominance of the Rhines scale $k_R \gg k_q$ predicts formation of zonal flows through turbulent inverse cascade. On the other hand, isotropic turbulence spectra are observed when the scale of quasi-crystallization dominates $k_q \gg k_R$.

With regard to the zonal flow generation, there are a number of studies based on modulational instability analyses, which are typically categorized into two classes: (i) parametric modulational instability analysis assuming the existence of a coherent primary wave (e.g., Ref. 6), or (ii) broad-band modulational instability analysis treated by the wave-kinetic equation with the scale separation assumption (e.g., Ref. 36). At the electron skin depth scale k_d, zonal flow generation could be weakened due to partial cancelation of the Reynolds stress by the Maxwell stress, as discussed in a work of parametric modulational instability analysis on the drift-Alfvén waves.[32] At the ion gyroradius scale k_i, the kinetic ion response could enhance the zonal flow generation rate as discussed in a work of parametric modulational instability analysis,[37] where the effects of electrostatic adiabatic/kinetic ion models on electron/ion-scale primary wave were examined.

Here, we evaluate the characteristic scales for the simulation results in Sec. III B. The scale of linear ETG mode is $k_l \sim 0.8\rho_{te}^{-1}$ from Fig. 1. With $U \sim 20\rho_{te}v_{te}/L_n$ for $\tilde{\phi} \sim 100\rho_{te}T_e/(eL_n)$ and $k_\perp \sim 0.2\rho_{te}^{-1}$ in Figs. 4 and 5, the Rhines scale is $k_R \sim 0.22\rho_{te}^{-1}$. The other three are determined only by plasma parameters: the scale of quasi-crystallization $k_q\rho_{te} \ll \sqrt{T_e/T_i} = 1$, the electron skin depth scale $k_d \sim d_e^{-1} = 0.045\rho_{te}^{-1}$, and the ion gyroradius scale $k_i \sim \rho_{ti}^{-1} = 0.036\rho_{te}^{-1}$. All scales are covered in the simulation box size ($L_x = 160\pi\rho_{te}$ so that $k_{\perp,\min} = 0.0125\rho_{te}^{-1}$). Comparing k_l, k_R, and k_q with the ETG turbulence spectra in the electrostatic adiabatic ion model [Fig. 5(a)], the void structure in the spectrum at low $k_\perp$ seems to close to the Rhines scale $k_\perp\rho_{te} \sim 0.2$. Then, the formation of zonal flows is also observed, which is consistent with Ref. 30. In the electromagnetic cases, weakening of zonal flow generation is observed in Fig. 5(c), although the wavenumber of zonal flows $k_\perp\rho_{te} \sim 0.2$ is relatively larger than the wavenumber of the electron skin depth $k_d\rho_{te} \sim 0.045$. In the electromagnetic kinetic ion simulation in Fig. 5(d), we do not observe the ion-scale zonal flows expected in Ref. 37. A possible explanation is that the turbulent inverse cascade was suspended at the Rhines scale, and thus, the primary wave at ion-scale was not excited in the simulation.

To quantify the effective mechanisms determining the ETG turbulence spectrum, parameter scans for k_l, k_R, k_q, k_d, and k_i are desired by changing, e.g., L_n^{-1}, T_e/T_i, β, and m_i/m_e, remain for future works.

IV. CONCLUSIONS

We have investigated the effects of kinetic ions and electromagnetic fluctuations on the slab ETG-driven turbulence based on the gyrokinetic theory and simulation. Although typical scales of the ETG instability are of the order of the electron gyroradius ρ_{te}, the nonadiabatic ion effect appears at the ion gyroradius scale $\rho_{ti} = \rho_{te}\sqrt{m_iT_i/(m_eT_e)}$, and the electromagnetic effect plays a role at the electron skin depth scale $d_e = \rho_{te}/\sqrt{\beta}$.

One of the important nonadiabatic ion effects is the ion polarization, which enhances the amplitude of electrostatic potential by reducing the dielectricity than that in the adiabatic ion model. It leads to destabilization of linear ETG modes at low $k_\perp$ ($\sim\rho_{ti}^{-1}$), and results in the extremely strong electron turbulent transport in the electrostatic limit. Enhancement of electrostatic potential by the ion polarization makes a finite difference in the heat transport between the electromagnetic adiabatic/kinetic ion models. The latter gives a slightly higher electron heat flux than the former.

The electromagnetic effect stabilizes the slab ETG instability at low $k_\perp$ ($\sim d_e^{-1}$), due to partial cancelation of parallel gradient of perturbed electron pressure by the electromagnetic diamagnetic term. The low-$k_\perp$ ETG instability with the ion polarization is stabilized when $\rho_{ti} \sim d_e$. In nonlinear turbulence, the electromagnetic effect weakens the zonal flow generation. Consequently, the resultant turbulent transport levels are found on the order of (electrostatic adiabatic ion model with strong zonal flows) $\ll$ (electromagnetic adiabatic ion model) $\lesssim$ (electromagnetic kinetic ion model with the ion polarization and the electromagnetic stabilization) $\ll$ (electrostatic kinetic ion model with destabilization of the low-k_y ETG modes by the ion polarization).

Since the enhancement of electrostatic potential by the ion polarization is a general consequence, and applicable not only to the shearless slab but also to the toroidal plasmas, a similar mechanism should work in toroidal ETG turbulence, while it has not been paid much attention in previous literature. Enhancement of linear growth rate of toroidal ETG mode by ion polarization is confirmed in our latest analysis.[38] Nonlinear turbulent flux, however, is reduced in kinetic ion cases than that in adiabatic ion cases,[8,38] in contrast to slab ETG turbulence. Furthermore, roles of electromagnetic fluctuations are also different; electromagnetic line-bending effect $\tilde{A}_\parallel$ tends to destabilize the toroidal ETG modes as β increases.[26] Magnetic compression $\tilde{B}_\parallel$ can also have stabilizing or destabilizing effects on toroidal ETG modes via the coupling with magnetic drift,[39] which is not expected in slab ETG modes. In addition, coupling with trapped electron dynamics makes the problem more complicated. Although the issues on the toroidal ETG turbulence has been an active research subject related to spherical tokamaks,[40–42] further studies are needed to better understand the full impact of kinetic ions and electromagnetic fluctuations on toroidal ETG turbulence.

ACKNOWLEDGMENTS

This work was partially supported by MEXT as "Program for Promoting Researches on the Supercomputer Fugaku" (Exploration of burning plasma confinement physics), JSPS KAKENHI Grant Nos. JP16H04086 and JP20K03892 "Joint Usage/Research Center for Interdisciplinary Large-Scale Information Infrastructures" and "High Performance Computing Infrastructure" (No. jh200053-MDHI), QST Research Collaboration for Fusion DEMO, and the NIFS Collaboration Research Program (Nos. NIFS18KNWT001 and NIFS20KNST162) in Japan. Numerical analyses were performed on the supercomputer Flow at Nagoya University, the JFRS-1 at Computational Simulation Centre of International Fusion Energy Research Centre (IFERC-CSC), and the Plasma simulator at National Institute for Fusion Science.

APPENDIX A: TWO-DIMENSIONAL SHEARLESS SLAB MODEL

A two-dimensional shearless slab model is employed in this paper, which was used in previous publications.[21,24,25] To reduce

the dimension, we restrict our analysis into the system having the translational symmetry $\partial_z = 0$. The magnetic field is almost aligned in the symmetric coordinate but slightly tilted $\boldsymbol{B} = B(\hat{\boldsymbol{z}} + \theta\hat{\boldsymbol{y}})$. Then, the field-aligned wavenumber is given by $k_\parallel = \boldsymbol{B}/B \cdot \boldsymbol{k} = \theta k_y$. Because the ratio $k_\parallel/k_y = \theta$ is fixed, this model is also called a non-resonant single helicity perturbation model.[29] Since the considered perpendicular wavelength is of the order of gyroradius $k_\perp \sim \rho^{-1}$, a typical parallel connection length $L_\parallel$ is characterized by $\theta = \rho/L_\parallel$, as drawn in Fig. 8. To satisfy the gyrokinetic ordering $k_\parallel/k_\perp \sim \rho/L_n \ll 1$, the tilt angle should be small as $\theta = \rho/L_\parallel \sim \rho/L_n \ll 1$. There are three geometrical parameters representing background scales, the scale lengths of density and temperature gradients L_n, L_{T_s}, and $L_\parallel$. In numerical simulation, we used L_n as the normalization length and treated $\Theta = L_n/L_\parallel$ and $\eta_s = L_n/L_{T_s}$ as parameters.

In this two-dimensional shearless slab system, the conventional delta-f gyrokinetic equations[22,23] (μ-dependence is still retained here, $\breve{f}_{s\boldsymbol{k}}(v_\parallel, \mu, t)$) are given by

$$\frac{\partial \breve{f}_{s\boldsymbol{k}}}{\partial t} + ik_\parallel v_\parallel \breve{f}_{s\boldsymbol{k}} = \frac{e_s F_{sM}}{T_s} J_{0s\boldsymbol{k}} \left[i\breve{\omega}_{*T_s} \left(\tilde{\phi}_{\boldsymbol{k}} - v_\parallel \tilde{A}_{\parallel\boldsymbol{k}} \right) - v_\parallel \left(ik_\parallel \tilde{\phi}_{\boldsymbol{k}} + \frac{\partial \tilde{A}_{\parallel\boldsymbol{k}}}{\partial t} \right) \right], \tag{A1}$$

$$0 = \sum_{s=e,i} e_s \left[\int J_{0s\boldsymbol{k}} \breve{f}_{s\boldsymbol{k}} dv^3 - \frac{e_s n}{T_s} (1 - \Gamma_{0s\boldsymbol{k}}) \tilde{\phi}_{\boldsymbol{k}} \right], \tag{A2}$$

$$k_\perp^2 \tilde{A}_{\parallel\boldsymbol{k}} = \mu_0 \sum_{s=e,i} e_s \int J_{0s\boldsymbol{k}} v_\parallel \breve{f}_{s\boldsymbol{k}} dv^3, \tag{A3}$$

where the nonlinear advection and collision terms are omitted for simplicity. The $\mu = m_s v_\perp^2/(2B)$ dependence appears in the background Maxwellian distribution $F_{sM} = F_{sM\parallel}(v_\parallel) F_{sM\perp}(v_\perp)$, the diamagnetic drift frequency $\breve{\omega}_{*T_s} = \omega_{*s}[1 + (\eta_s/2)(m_s(v_\parallel^2 + v_\perp^2)/T_s - 3)]$, and the gyroaverage operator $J_{0s\boldsymbol{k}} = J_0(k_\perp \rho_s)$ with the zeroth-order Bessel function J_0 and $\rho_s = m_s v_\perp/(e_s B)$.

From Eq. (A1), the linear response of gyrocenter distribution is obtained as

$$\breve{f}_{s\boldsymbol{k}} = -J_{0s\boldsymbol{k}} \frac{e_s F_{sM}}{T_s} \left[\tilde{\phi}_{\boldsymbol{k}} - \frac{\omega - \breve{\omega}_{*T_s}}{\omega - k_\parallel v_\parallel} \left(\tilde{\phi}_{\boldsymbol{k}} - v_\parallel \tilde{A}_{\parallel\boldsymbol{k}} \right) \right]. \tag{A4}$$

Substituting the above into Eqs. (A2) and (A3), one derives the linear dispersion relation

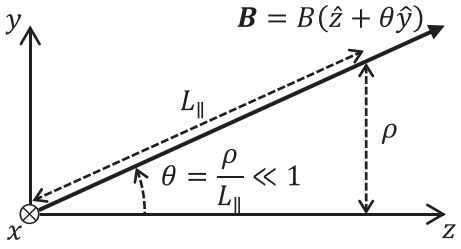

FIG. 8. Two-dimensional shearless slab model geometry. Translational symmetry $\partial_z = 0$ is also imposed.

$$\left[\sum_{s=e,i} \frac{2\alpha_s^2}{k_\perp^2 d_s^2} \left(1 - \breve{G}_{0s} \right) \right] \left[1 + \sum_{s=e,i} \frac{2\alpha_s^2}{k_\perp^2 d_s^2} \breve{G}_{2s} \right] + \left[\sum_{s=e,i} \frac{2\alpha_s^2}{k_\perp^2 d_s^2} \breve{G}_{1s} \right]^2 = 0, \tag{A5}$$

$$\breve{G}_{js} = \int J_{0s\boldsymbol{k}}^2 \frac{\omega - \breve{\omega}_{*T_s}}{\omega - k_\parallel v_\parallel} \frac{F_{sM}}{n} \left(\frac{k_\parallel v_\parallel}{\omega} \right)^j dv^3. \tag{A6}$$

Explicitly writing down $\breve{G}_{js}$

$$\breve{G}_{1s} = \breve{G}_{2s} = \breve{G}_{0s} - \Gamma_{0s\boldsymbol{k}} \left[1 - \frac{\omega_{*s}}{\omega} \left(1 - \frac{\eta_s \breve{b}_{s\boldsymbol{k}}}{2} \right) \right], \tag{A7}$$

$$\breve{G}_{0s} = \Gamma_{0s\boldsymbol{k}} \Big\{ -\alpha_s Z(\alpha_s) + \alpha_{*s} Z(\alpha_s) + \alpha_{*T_s} \left[\alpha_s (1 + \alpha_s Z(\alpha_s)) - \frac{1}{2} \left(1 + \breve{b}_{s\boldsymbol{k}} \right) Z(\alpha_s) \right] \Big\}, \tag{A8}$$

where $\breve{b}_{s\boldsymbol{k}} = 2b_{s\boldsymbol{k}}(1 - I_{1s\boldsymbol{k}}/I_{0s\boldsymbol{k}})$ with $I_{js\boldsymbol{k}} = I_j(b_{s\boldsymbol{k}})$ and the jth-order modified Bessel function I_j. The normalized frequencies are given by $\alpha_s = \omega/\left(\sqrt{2}k_\parallel v_{ts}\right)$, $\alpha_{*s} = \omega_{*s}/\left(\sqrt{2}k_\parallel v_{ts}\right)$ and $\alpha_{*T_s} = \eta_s \alpha_{*s}$, and the plasma dispersion function is denoted by Z.

APPENDIX B: PERPENDICULAR VELOCITY SPACE CLOSURE

To reduce the dimension further, we have assumed the perpendicular velocity dependence to be a Maxwell distribution $\breve{f}_{s\boldsymbol{k}}(v_\parallel, \mu, t) \to \tilde{f}_{s\boldsymbol{k}}(v_\parallel, t) F_{sM\perp}(\mu)$. Taking the perpendicular velocity space integral $^- = \int d\mu 2\pi B/m_s$ of Eq. (A1) and using the mathematical formulas $\overline{J_{0s\boldsymbol{k}} F_{sM\perp}} = e^{-b_{s\boldsymbol{k}}/2}$, one derives Eqs. (4)–(10) in Sec. II. This approach reduces computational cost of numerical simulation, while the modified gyroaveraging factor $e^{-b_{s\boldsymbol{k}}/2}$ causes a slight difference in linear dispersion relation. This is a known problem when developing a gyrofluid model. One approach to resolve this problem is a particle position moment approach, and another is a gyrocenter moment expansion with $\overline{J_{0s\boldsymbol{k}} F_{sM\perp}} \sim \sqrt{\Gamma_{0s\boldsymbol{k}}}$ approximation.[43] See Refs. 43 and 44 for more details. In this Appendix, we explain how linear dispersion relations in full gyrokinetic equations, Eq. (A5), and in the perpendicular Maxwellian model, Eq. (B2), are different.

Neglecting $N_{s\boldsymbol{k}}$ and $C_{s\boldsymbol{k}}$ from Eqs. (4), one derives the linear response of gyrocenter distribution as

$$\tilde{f}_{s\boldsymbol{k}} = -e^{-b_{s\boldsymbol{k}}/2} \frac{e_s F_{sM\parallel}}{T_s} \left[\tilde{\phi}_{\boldsymbol{k}} - \frac{\omega - \omega_{*T_s}}{\omega - k_\parallel v_\parallel} \left(\tilde{\phi}_{\boldsymbol{k}} - v_\parallel \tilde{A}_{\parallel\boldsymbol{k}} \right) \right]. \tag{B1}$$

We note that perpendicular velocity space has already been integrated out. Substituting the above into Eqs. (7) and (9), one derives the linear dispersion relation for the model in Sec. II

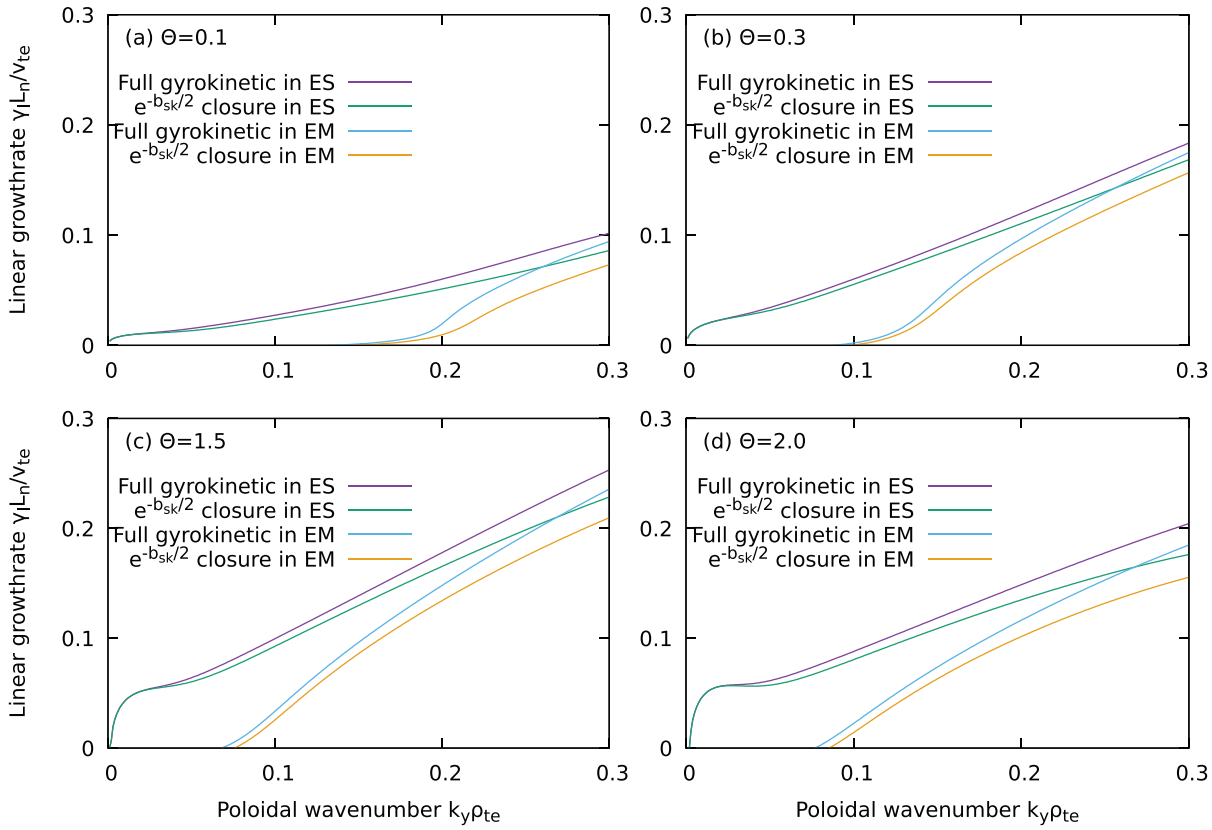

FIG. 9. Linear growth rate γ_l as functions of the poloidal wavenumber k_y. Violet, green, cyan, and orange lines correspond to the results given by electrostatic full gyrokinetic model [Eq. (A5) with $\beta = 0$], electrostatic perpendicular Maxwellian ($e^{-b_{sk}/2}$ closure) model [Eq. (B2) with $\beta = 0$], electromagnetic full gyrokinetic model [Eq. (A5)], electromagnetic perpendicular Maxwellian ($e^{-b_{sk}/2}$ closure) model [Eq. (B2)], respectively. Panels (a)–(d) change the tilt angle as $\Theta = 0.1, 0.3, 1.5$, and 2.0.

$$\left[\sum_{s=e,i}\frac{2\alpha_s^2}{k_\perp^2 d_s^2}\left(1-\Gamma_{0sk}+e^{-b_{sk}}-G_{0s}\right)\right]\left[1+\sum_{s=e,i}\frac{2\alpha_s^2}{k_\perp^2 d_s^2}G_{2s}\right] + \left[\sum_{s=e,i}\frac{2\alpha_s^2}{k_\perp^2 d_s^2}G_{1s}\right]^2 = 0, \tag{B2}$$

$$G_{js} = e^{-b_{sk}}\int\frac{\omega-\omega_{*T_s}}{\omega-k_\parallel v_\parallel}\frac{F_{sM\parallel}}{n}\left(\frac{k_\parallel v_\parallel}{\omega}\right)^j dv_\parallel, \tag{B3}$$

where

$$G_{1s} = G_{2s} = G_{0s} - e^{-b_{sk}}\left[1-\frac{\omega_{*s}}{\omega}\left(1-\frac{\eta_s b_{sk}}{2}\right)\right], \tag{B4}$$

$$G_{0s} = e^{-b_{sk}}\Big\{-\alpha_s Z(\alpha_s)+\alpha_{*s}Z(\alpha_s) + \alpha_{*T_s}\left[\alpha_s(1+\alpha_s Z(\alpha_s))-\frac{1}{2}(1+b_{sk})Z(\alpha_s)\right]\Big\}. \tag{B5}$$

Comparing Eqs. (A5) and (B2), differences are $e^{-b_{sk}} \to \Gamma_{0sk}$ and $b_{sk} \to \tilde{b}_{sk} = 2b_{sk}(1 - I_{1sk}/I_{0sk})$. Because these difference could be non-negligible at small wavelengths, we should check whether these differences change the ion finite Larmor radius effects on ETG modes.

The linear dispersion relations obtained from the gyrokinetic equations with full μ dependence, Eq. (A5), and from the perpendicular Maxwellian model, Eq. (B2), are compared in Fig. 9. The growth rate around $k_y\rho_{te} < 0.05$ are enhanced by ion finite Larmor radius effects in both of electrostatic full gyrokinetic and perpendicular Maxwellian models. Stabilization by electromagnetic fluctuations also shows quantitative agreement. The destabilization by ion FLR and stabilization by electromagnetic fluctuations are observed in all cases in Fig. 9 independent to the choice of tilt angle Θ.

APPENDIX C: LINEAR DISPERSION RELATION OF SLAB ETG FROM FLUID DESCRIPTION

As discussed in Sec. III A, the linear dispersion relation of slab ETG instability is understood in the electron fluid approximation $k_\parallel v_\parallel \ll \omega$, which drops contributions from higher-order $v_\parallel$ moments. Relations between kinetic and fluid equations for electrostatic drift waves are described in Ref. 45. For the ETG modes including electromagnetic fluctuations, a kinetic dispersion in Ref. 26 can be reduced to fluid equations in Ref. 13. In this Appendix, we summarize a set of fluid equations for the slab ETG instability in the electron gyroradius scale, including the ion FLR effects and electromagnetic fluctuations.

Considering a flat density profile ($\nabla n = 0$) but with a finite temperature gradient ($\nabla P_e = -\hat{\boldsymbol{x}} n T_e / L_{T_e}$) in a homogeneous equilibrium magnetic field, one describes a set of electron fluid equations. The continuity equation involves the parallel compression

$$-i\omega\tilde{n}_{e\boldsymbol{k}} = -ink_\parallel \tilde{v}_{\parallel e\boldsymbol{k}}. \tag{C1}$$

Forces in the equation of motion are the parallel gradient of perturbed pressure, gradient of the equilibrium pressure along perturbed magnetic field (electromagnetic diamagnetic term), and the electrostatic and induced parallel electric fields

$$-i\omega m_e n\tilde{v}_{\parallel e\boldsymbol{k}} = -ik_\parallel \tilde{p}_{e\boldsymbol{k}} + ien\omega_{*T_e}\tilde{A}_{\parallel\boldsymbol{k}} + en\left(ik_\parallel\tilde{\phi}_{\boldsymbol{k}} - i\omega\tilde{A}_{\parallel\boldsymbol{k}}\right). \tag{C2}$$

Neglecting the parallel heat flux, the pressure equation is given by $E \times B$ advection of the equilibrium pressure

$$-i\omega\tilde{p}_{e\boldsymbol{k}} = -ien\omega_{*T_e}\tilde{\phi}_{\boldsymbol{k}}. \tag{C3}$$

Electromagnetic potentials are determined by the quasi-neutrality and the Ampère equations

$$\tilde{n}_{e\boldsymbol{k}} = \tilde{n}_{i\boldsymbol{k}}, \tag{C4}$$

$$k_\perp^2 \tilde{A}_{\parallel\boldsymbol{k}} = -\mu_0 en\tilde{v}_{\parallel e\boldsymbol{k}}, \tag{C5}$$

where the ion parallel current is neglected. The ion particle-position density consists of the ion polarization and the ion gyrocenter density $\tilde{n}_{i\boldsymbol{k}}^{(gc)}$

$$\tilde{n}_{i\boldsymbol{k}} = -(1-\Gamma_{0i\boldsymbol{k}})\frac{en}{T_i}\tilde{\phi}_{\boldsymbol{k}} + \tilde{n}_{i\boldsymbol{k}}^{(gc)}. \tag{C6}$$

In the continuity equation of gyrocenter density, the ion parallel motion is negligible at electron gyroradius scale. Even in a flat density profile, the ion diamagnetic term survives due to the ion FLR effects

$$\frac{\partial\tilde{n}_{i\boldsymbol{k}}^{(gc)}}{\partial t} = -i\frac{\omega_{*T_i}\breve{b}_{i\boldsymbol{k}}}{2}\Gamma_{0s\boldsymbol{k}}\frac{en}{T_i}\tilde{\phi}_{\boldsymbol{k}}, \tag{C7}$$

when there is the ion temperature gradient. Substituting all others into the equation of motion, one finds

$$-\tau = \frac{k_\parallel^2 v_{te}^2}{\omega^2}\frac{\omega_{*T_e}}{\omega} - \frac{\omega_{*T_e}}{\omega}\frac{\mu_0 e^2 n}{k_\perp^2 m_e}\tau - \frac{k_\parallel^2 v_{te}^2}{\omega^2} - \frac{\mu_0 e^2 n}{k_\perp^2 m_e}\tau, \tag{C8}$$

where the terms in the same order of Eq. (C2) are retained. The ion nonadiabatic FLR effects are represented in $\tau = \{1-\Gamma_{0i\boldsymbol{k}}[1+\omega_{*T_i}\breve{b}_{i\boldsymbol{k}}/(2\omega)]\}T_e/T_i$. After normalization, it reads

$$-\tau = \frac{1}{2\alpha_e^2}\frac{\alpha_{*T_e}}{\alpha_e} - \frac{\alpha_{*T_e}}{\alpha_e}\frac{1}{k_\perp^2 d_e^2}\tau - \frac{1}{2\alpha_e^2} + \frac{1}{k_\perp^2 d_e^2}\tau, \tag{C9}$$

where one finds correspondence of each term in the equation of motion (C2) and the fluid limit of the linear dispersion relation, Eq. (21).

DATA AVAILABILITY

The data that support the findings of this study are available from the corresponding author upon reasonable request.

REFERENCES

[1] B. W. Stallard, C. M. Greenfield, G. M. Staebler, C. L. Rettig, M. S. Chu, M. E. Austin, D. R. Baker, L. R. Baylor, K. H. Burrell, J. C. DeBoo, J. S. deGrassie, E. J. Doyle, J. Lohr, G. R. McKee, R. L. Miller, W. A. Peebles, C. C. Petty, R. I. Pinsker, B. W. Rice, T. L. Rhodes, R. E. Waltz, L. Zeng, and T. D.-D. Team, Phys. Plasmas **6**, 1978 (1999).
[2] L. I. Rudakov and R. Z. Sagdeev, Dokl. Akad. Nauk SSSR **128**, 581 (1961) [Sov. Phys. Dokl. **6**, 415 (1961)].
[3] O. P. Pogutse, Plasma Phys. **10**, 649 (1968).
[4] W. Horton, Rev. Mod. Phys. **71**, 735 (1999).
[5] W. Dorland, F. Jenko, M. Kotschenreuther, and B. N. Rogers, Phys. Rev. Lett. **85**, 5579 (2000).
[6] F. Jenko, W. Dorland, M. Kotschenreuther, and B. N. Rogers, Phys. Plasmas **7**, 1904 (2000).
[7] G. J. Colyer, A. A. Schekochihin, F. I. Parra, C. M. Roach, M. A. Barnes, Y. C. Ghim, and W. Dorland, Plasma Phys. Controlled Fusion **59**, 055002 (2017).
[8] J. Candy, R. E. Waltz, M. R. Fahey, and C. Holland, Plasma Phys. Controlled Fusion **49**, 1209 (2007).
[9] T. Görler and F. Jenko, Phys. Rev. Lett. **100**, 185002 (2008).
[10] S. Maeyama, Y. Idomura, T.-H. Watanabe, M. Nakata, M. Yagi, N. Miyato, A. Ishizawa, and M. Nunami, Phys. Rev. Lett. **114**, 255002 (2015).
[11] N. T. Howard, C. Holland, A. E. White, M. Greenwald, and J. Candy, Nucl. Fusion **56**, 014004 (2016).
[12] M. R. Hardman, M. Barnes, and C. M. Roach, J. Plasma Phys. **86**, 905860601 (2020).
[13] W. Horton, B. G. Hong, and W. M. Tang, Phys. Fluids **31**, 2971 (1988).
[14] R. Singh, H. Jhang, and P. H. Diamond, Phys. Plasmas **20**, 112506 (2013).
[15] T. Ohkawa, Phys. Lett. A **67**, 35 (1978).
[16] W. M. Nevins, J. Candy, S. Cowley, T. Dannert, A. Dimits, W. Dorland, C. Estrada-Mila, G. W. Hammett, F. Jenko, M. J. Pueschel, and D. E. Shumaker, Phys. Plasmas **13**, 122306 (2006).
[17] A. M. Dimits, W. M. Nevins, D. E. Shumaker, G. W. Hammett, T. Dannert, F. Jenko, M. J. Pueschel, W. Dorland, S. C. Cowley, J. N. Leboeuf, T. Rhodes, J. Candy, C. Estrada-Mila, W. Horton, B. G. Hong, and W. M. Tang, Nucl. Fusion **47**, 817 (2007).
[18] S. Yi, H. Jhang, and J. M. Kwon, Phys. Plasmas **23**, 102514 (2016).
[19] Y. Idomura, S. Tokuda, and Y. Kishimoto, Nucl. Fusion **45**, 1571 (2005).
[20] J. F. Parisi, F. I. Parra, C. M. Roach, C. Giroud, W. Dorland, D. R. Hatch, M. Barnes, J. C. Hillesheim, N. Aiba, and J. Ball, Nucl. Fusion **60**, 126045 (2020).
[21] M. Nakata, T.-H. Watanabe, H. Sugama, and W. Horton, Phys. Plasmas **17**, 042306 (2010).
[22] E. A. Frieman and L. Chen, Phys. Fluids **25**, 502 (1982).
[23] W. W. Lee, Phys. Fluids **26**, 556 (1983).
[24] T.-H. Watanabe and H. Sugama, Phys. Plasmas **11**, 1476 (2004).
[25] A. Ishizawa, T.-H. Watanabe, and N. Nakajima, Plasma Fusion Res. **6**, 2403087 (2011).
[26] J. Y. Kim and W. Horton, Phys. Fluids B **3**, 3194 (1991).
[27] Y. C. Lee, J. Q. Dong, P. N. Guzdar, and C. S. Liu, Phys. Fluids **30**, 1331 (1987).
[28] B. B. Kadomtsev and O. P. Pogutse, *Reviews of Plasma Physics* (Consultants Bureau, New York, 1970), p. 309.
[29] Y. Idomura, Phys. Plasmas **13**, 080701 (2006).
[30] C. Kawai, Y. Idomura, S. Maeyama, and Y. Ogawa, Phys. Plasmas **24**, 042303 (2017).
[31] P. H. Diamond, S.-I. Itoh, K. Itoh, and T. S. Hahm, Plasma Phys. Controlled Fusion **47**, R35 (2005).
[32] P. N. Guzdar, R. G. Kleva, A. Das, and P. K. Kaw, Phys. Plasmas **8**, 3907 (2001).
[33] A. Hasegawa and K. Mima, Phys. Rev. Lett. **39**, 205 (1977).
[34] G. K. Vallis and M. E. Maltrud, J. Phys. Oceanogr. **23**, 1346 (1993).
[35] T. Watanabe, H. Fujisaka, and T. Iwayama, Phys. Rev. E **55**, 5575 (1997).
[36] A. I. Smolyakov, P. H. Diamond, and M. Malkov, Phys. Rev. Lett. **84**, 491 (2000).
[37] G. Plunk, Phys. Plasmas **14**, 112308 (2007).
[38] T.-H. Watanabe, S. Kusaka, T. Oguri, and S. Maeyama, in Proceedings of 28th IAEA Fusion Energy Conference (2021), p. 826.
[39] N. Joiner and A. Hirose, Phys. Plasmas **14**, 112111 (2007).
[40] N. Joiner, D. Applegate, S. C. Cowley, W. Dorland, C. M. Roach, N. Joiner, and A. Hirose, Plasma Phys. Controlled Fusion **48**, 685 (2006).

[41]C. M. Roach, I. G. Abel, R. J. Akers, W. Arter, M. Barnes, Y. Camenen, F. J. Casson, G. Colyer, J. W. Connor, S. C. Cowley, D. Dickinson, W. Dorland, A. R. Field, W. Guttenfelder, G. W. Hammett, R. J. Hastie, E. Highcock, N. F. Loureiro, A. G. Peeters, M. Reshko, S. Saarelma, A. A. Schekochihin, M. Valovic, and H. R. Wilson, Plasma Phys. Controlled Fusion **51**, 124020 (2009).
[42]W. Guttenfelder and J. Candy, Phys. Plasmas **18**, 022506 (2011).
[43]W. Dorland and G. W. Hammett, Phys. Fluids B **5**, 812 (1993).
[44]B. Scott, Phys. Plasmas **17**, 102306 (2010).
[45]B. Coppi, M. N. Rosenbluth, and R. Z. Zagdeev, Phys. Fluids **10**, 582 (1967).